This article is made available for a limited time sponsored by ACS under the ACS Free to Read License, which permits copying and redistribution of the article for non-commercial scholarly purposes.

ACS APPLIED ENERGY MATERIALS

Article

Cite This: ACS Appl. Energy Mater. 2019, 2, 905−912

www.acsaem.org

Compact Lithium-Ion Battery Electrodes with Lightweight Reduced Graphene Oxide/Poly(Acrylic Acid) Current Collectors

Joshua P. Pender,[†] Han Xiao,[§] Ziyue Dong,[‡] Kelsey A. Cavallaro,[‡] Jason A. Weeks,[†] Adam Heller,[‡] Christopher J. Ellison,*[,§] and C. Buddie Mullins*[,†,‡]

[†]Department of Chemistry and [‡]John J. Mcketta Department of Chemical Engineering, The University of Texas at Austin, Austin, Texas 78712, United States

[§]Department of Chemical Engineering and Materials Science, The University of Minnesota, Minneapolis, Minnesota 55455, United States

Supporting Information

ABSTRACT: We report the fabrication and electrochemical performance of metal-foil free $Li_4Ti_5O_{12}$ (LTO) and $LiNi_{1/3}Co_{1/3}Mn_{1/3}O_2$ (NCM) electrodes supported on conductive and porous reduced graphene oxide/poly(acrylic acid) (rGO-PAA) aerogels. The highly porous rGO-PAA (~6 mg cm^{-3}) enables slurry infiltration of LTO and NCM to form composite electrodes with tunable mass loadings (~3−30 mg cm^{-2}), and the resultant composites can withstand 100-fold compression (from 3.2 mm to ~30−130 μm) to achieve electrode densities of 2−3 g cm^{-3}. The adequate compressibility of the rGO-PAA coupled with removal of the conventional metal-foil weight and volume provides high volumetric energy densities of 1723 Wh L^{-1} for NCM and 625 Wh L^{-1} for LTO at low power density, representing a 25% increase in energy density over similar electrodes built with metal-foil current collectors. These metrics demonstrate the utility of the rGO-PAA current collector to reduce the weight and volume of lithium-ion electrodes without sacrificing energy density.

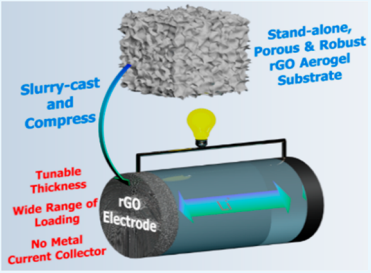

KEYWORDS: *3D electrode, reduced graphene oxide, aerogel, lithium ion battery, volumetric energy density*

1. INTRODUCTION

In conventional lithium ion batteries (LIBs) with metal-foil current collectors, the volumetric and gravimetric energy densities are reduced by their inactive film additives for conduction and binding, separators, and current collectors.[1−9] The losses in energy density are mitigated upon increasing the mass loading (thickness) of the electroactive layer such that the mass and the volume of the current collector and separator are reduced. However, concentration polarization due to inadequate Li^+ diffusion reduces the electrolyte-accessible depth of the electroactive layer and has thus far restricted electrode thickness to ~100−125 μm. Thicker electroactive layers are also fragile, cracking, and potentially delaminating from the current collector upon their volume changes during cycling. The associated engineering challenges have motivated studies aimed at improving the performance of thick electrodes with high active material loadings.[3−9]

Part of these limitations are overcome upon substituting the slurry-coated metal-foil current collectors by porous, free-standing, conductive, and elastic composites with high mechanical durability. This change eliminates the metal foil weight and volume, and the integrated architecture allows for deformation during cycling with mitigated structural deterioration.[10−12] Composite electrodes with active material loadings of >10 mg cm^{-2} have been reported with porous metals,[13−16] with elastomeric substrates,[17,18] and with porous carbon substrates fabricated from carbon nanotubes (CNTs), graphene derivatives, cellulose, or carbon textiles.[18−30] Frameworks fabricated from CNTs and graphene derivatives have received particular attention in both conventional electrode architectures and conversion/alloy electrodes (e.g., Li−S), owing to their excellent mechanical properties and high electrical conductivities.[10−12,30−32] Notably, Zhou et al. fabricated a free-standing, AlF_3-coated CNT/nanofibrillar cellulose/$LiCoO_2$ composite using vacuum filtration followed by atomic layer deposition.[23] They achieved an active material loading of ~20 mg cm^{-2} and demonstrated the increase in energy density upon eliminating the metal-foil current collector. Additionally, an AlF_3-coating provided an increase in the operating voltage to 4.7 V, greatly improving the energy density of the $LiCoO_2$ cathode. However, the required atomic layer deposition may hinder the commercial scalability. In another report, Chen et al. used carbonized natural wood to fabricate a thick composite $LiFePO_4$ (LFP) electrode (~800 μm) with a mass loading of ~60 mg cm^{-2}.[27] The LFP composite was fabricated by infiltrating an epoxy/LFP mixture, followed by removal of the epoxy resin by calcination. This composite delivered a high areal capacity of 7.6 mAh cm^{-2} at 0.5 mA cm^{-2}, but the natural wood composite could not be compressed below ~800 μm and thus the electrode had a

Received: November 19, 2018
Accepted: December 28, 2018
Published: December 28, 2018

Downloaded via UNIV OF TEXAS AT AUSTIN on January 29, 2019 at 14:11:11 (UTC).
See https://pubs.acs.org/sharingguidelines for options on how to legitimately share published articles.

© 2018 American Chemical Society

DOI: 10.1021/acsaem.8b02007
ACS Appl. Energy Mater. 2019, 2, 905−912

relatively low volumetric energy density (323 Wh L^{-1}), hindering its utility in volume-confined applications. Although dense LIB electrodes with high active-material loadings have been greatly improved, their fabrication for applications where a small volume is of essence remains a challenge.[10−12]

We have previously reported the synthesis (starting from graphite and poly(acrylic acid) (PAA)) and electrical/structural characterization of a thermally cross-linked, reduced graphene oxide/poly(acrylic acid) (rGO-PAA) aerogel substrate.[19,33] When applied as a free-standing, 3D current collector in LIBs, the highly porous rGO-PAA substrate can increase the effective electrode−electrolyte contact area 2.5-fold by increasing the electrode surface roughness and thus improving the lithiation/delithiation kinetics of a commercial LFP cathode.[19] This previous study focused on minimizing the inactive material content with a relatively limited range of LFP loadings (9 and 16 mg cm^{-2}), composite thicknesses, and electrode densities.

As model materials to investigate the utility of our 3D rGO-PAA current collector to fabricate compact composite electrodes, we chose commercially available $LiNi_{1/3}Co_{1/3}Mn_{1/3}O_2$ (NCM) because of its high energy and power densities and increasing commercial interest,[7,34,35] while $Li_4Ti_5O_{12}$ (LTO) was selected due to its excellent safety, relatively low cost, minimal volume change during lithiation/delithiation, and relatively high operating voltage versus Li/Li^+ that motivates the need for higher energy density LTO-based systems.[36] By switching from conventional metal-foil current collectors to the 3D rGO-PAA scaffold, we demonstrate here a substantial increase in achievable volumetric energy density for both LTO and NCM at comparable active material loadings (~3−30 mg cm^{-2}) and thicknesses (~30−130 μm).

2. EXPERIMENTAL SECTION

2.1. Fabrication of rGO-PAA Aerogel Substrates. Graphene oxide (GO) was produced using a modified Hummers method similar to the procedures described in our previous report.[19] Briefly, potassium permanganate and sulfuric acid was used to further oxidize graphite powder (SP-1, Bay Carbon Inc.) to GO. The GO was later isolated from the acid by washing with an excessive amount of water and then freeze-dried to obtain a GO aerogel that was a convenient form for later handling. The freeze-dried GO was then redispersed in DI water (5 mg mL^{-1}) with PAA (Sigma-Aldrich; M_v = 450 000 g/mol) in a 2:1 weight ratio with rapid stirring to dissolve the PAA (1000 rpm for 10 min), followed by probe sonication using a 400 W probe sonicator (1/8″ probe; Branson Digital Sonifier 450) with 10% amplitude for 10 min (24 kJ) in an ice bath to exfoliate GO and promote a homogeneous solution. The GO-PAA aqueous dispersion was poured into poly(dimethylsiloxane) molds (Sylgard 184, 10:1 elastomer/curing agent) and freeze-dried by immersion in liquid nitrogen for 5 min followed by transfer of the solid sample to a vacuum chamber at room temperature for 24 h. The free-standing GO-PAA aerogel bars were then reduced by HI vapor treatment at room temperature for 24 h and then annealed at 160 °C under vacuum to remove residual HI and simultaneously thermally cross-link the PAA polymer chains to poly(acrylic anhydrides). It is expected that further reduction of GO to rGO could occur during this step.

2.2. Characterization. The size distribution of the GO platelets was investigated using an atomic force microscope (AFM; Nanoscope V Multimode 8) equipped with Peak Force QNM tapping mode and Al-coated Si cantilevers (HQ: NSC36/AL BS, Micro Masch, nominal force constant = 0.6 N/m). To prepare samples for AFM characterization, 10 mL of GO solution (5 mg mL^{-1}) was probe sonicated (400 W; 1/8″ probe; Branson Digital Sonifier 450) at 10% amplitude for 10 min (24 kJ) in an ice bath to promote a homogeneous solution (consistent with aerogel synthesis procedure). One hundred microliters of this solution was then transferred to a new vial and diluted to a final volume of 10 mL with DI water for a GO concentration 0.05 mg mL^{-1} (dilution was performed to avoid agglomeration and overlap of GO sheets). The diluted GO solution was then well-mixed using a vortex mixer at 2500 rpm for 2 min and spin-coated onto a silicon wafer that was pretreated with Piranha solution. The degree of oxidation of the GO was measured using X-ray photoelectron spectroscopy (XPS, SSX-100). X-ray diffraction patterns were recorded on a Rigaku Miniflex 600 diffractometer using monochromatic Cu Kα radiation (λ = 1.5418 Å). X-ray patterns were measured in the 5−50° 2θ range in a continuous scan mode (1° min^{-1}) with a step width of 2θ = 0.025°. Raman spectra were recorded with a Witec Micro-Raman Alpha 300 Spectrometer using a Witec 40W (60 Hz), 488 nm (2.54 eV, blue) laser. For all Raman measurements, a Nikon E Plan camera with a 20× objective was used at a working distance of 3.8 cm. Thermogravimetric analysis (TGA; Mettler Toledo TGA/DSC 1StAR^e system) was conducted under N_2 (flow rate = 50 mL min^{-1}). The TGA experiments were conducted from room temperature to 100 °C and held for 15 min to remove moisture and adsorbed gases, followed by ramping to 800 °C at 10 °C min^{-1}. Mechanical stress−strain measurements were made using a rheometer (TA Instrument, RSA-G2). Scanning electron microscopy (SEM) images were collected using a FEI Quanta 650 ESEM equipped with an energy-dispersive X-ray (EDX) detector.

2.3. Electrochemical Measurements. Commercially available NCM and LTO active materials were purchased from MTI Corporation for electrochemical testing (SEM images in Figure S20). The NCM has a mean particle size of 9−12 μm and a tap density of 2.30 g cm^{-3}, and the LTO has a mean particle size of 1.1 μm and a tap density of 1.5 g cm^{-3}. The composite electrodes were fabricated by mixing LTO or NCM with Super P conductive carbon (MTI) and polyvinylidene fluoride (PVDF, MTI) in an 86:7:7 ratio with *N*-methyl-2-pyrrolidone (NMP, Sigma-Aldrich) solvent and cast onto either the rGO-PAA substrate (NCM-rGO or LTO-rGO) or onto Al-foil (NCM-Al) or Cu-foil (LTO-Cu). For the rGO-PAA electrodes, the composites were rolled onto filter paper to remove excess slurry coating the substrate surface prior to drying under vacuum at 80 °C for 16 h. Each respective electrode was then weighed and compressed using a calender (MRX-SG100L, Polaris Battery Laboratories). The thickness of each electrode was measured using a digital micrometer with ±1 μm resolution (Mitutoyo 293 series). To identify a specific electrode, we have adopted the following nomenclature: active material-current collector-thickness. For example, LTO-rGO-31 refers to an LTO@rGO-PAA composite electrode calendered to 31 μm, and NCM-Al-62 refers to an NCM@Al foil electrode calendered to an electroactive film-thickness of 62 μm. An overview of the electrodes tested here is presented in Table 1a (LTO) and Table 1b (NCM). The composite NCM and LTO electrodes were assembled into standard CR2032 coin cells with lithium foil (Alfa Aesar, 99.9%) as the counter electrode, a Celgard 2400 polypropylene separator, and 1.2 M $LiPF_6$ in 3:7 Ethylene Carbonate (EC): dimethyl carbonate (DMC) (v/v) as the electrolyte and allowed to rest at open circuit voltage for 12 h. Cyclic voltammetry (CV) and galvanostatic charge−discharge tests were performed on a 40-channel battery analyzer (BT2043, Arbin). In all tests, three conditioning cycles at 0.05C were performed to ensure adequate electrolyte wetting and utilization of the active materials, followed by cycling between 3.0−4.3 V vs Li/Li^+ for NCM electrodes (1 C = 160 mA g^{-1}) and 1.0−2.5 V vs Li/Li^+ for LTO electrodes (1 C = 175 mA g^{-1}). Electrochemical impedance spectroscopy (EIS) was conducted between 10 mHz−100 kHz with an amplitude of 5 mV using a potentiostat/galvanostat (CH 680D, CH Instruments).

3. RESULTS AND DISCUSSION

The procedure for forming the porous and elastomeric rGO-PAA from GO is outlined in Figure 1a. The GO aerogel (Figure 1b), obtained by freeze-drying an aqueous GO suspension, is comprised of randomly oriented and poorly

DOI: 10.1021/acsaem.8b02007
ACS Appl. Energy Mater. 2019, 2, 905−912

Table 1. (a) LTO-rGO and LTO-Cu Electrodes and (b) NCM-rGO and NCM-Al Electrodes[a]

(a)				
electrode ID	composite film thickness (μm)	LTO loading (mg cm^{-2})	LTO (wt %)	composite density (g cm^{-3})
LTO-rGO-31	31	3.0	60	1.61
LTO-rGO-80	80	12.8	78	2.04
LTO-rGO-102	102	16.5	80	2.04
LTO-rGO-125	125	23.4	82	2.27
LTO-Cu-30	30 (+11)	2.7	23	3.05
LTO-Cu-78	78 (+11)	12.7	51	2.64
LTO-Cu-102	102 (+11)	16.4	57	2.52
LTO-Cu-123	123 (+11)	20.1	61	2.45
(b)				
electrode ID	composite film thickness (μm)	NCM loading (mg cm^{-2})	NCM (wt %)	composite density (g cm^{-3})
NCM-rGO-29	29	3.7	64	2.00
NCM-rGO-65	65	12.4	73	2.45
NCM-rGO-96	96	20.3	81	2.62
NCM-rGO-129	129	31.9	83	2.99
NCM-Al-29	29 (+16)	3.6	42	1.92
NCM-Al-62	62 (+16)	12.2	65	2.38
NCM-Al-94	94 (+16)	19.9	72	2.51
NCM-Al-127	127 (+16)	29.9	76	2.74

[a]The numbers in parentheses represent the thicknesses of Cu foil (LTO) or Al foil (NCM).

interconnected GO platelets (atomic force microscopy analysis of GO platelets shown in Figure S1). As seen in Figure 1c, the addition of PAA to the GO suspension promotes the formation of an extended, well-interconnected architecture due to the strong interaction between GO and PAA.[33] Subsequent reduction of the GO-PAA by HI vapor and thermal cross-linking at 160 °C provides the rGO-PAA with pore diameters of ≥10 μm (Figure 1d; Figure S2) that provide an adequate template for electrolyte transport following compression.

XPS spectra confirm that GO is reduced to rGO by HI vapor and thermal annealing. The XPS survey spectra of GO (black trace) and rGO (red trace) are consistent with reduction of GO to rGO, the reduction evidenced by the decrease in the O/C ratio from 0.55 to 0.24 (Figure 1e). The C 1s spectrum of GO (Figure 1f) shows three types of carbon, their respective binding energies consistent with those of C−C and C═C (~284.7 eV), C−O (~286.7 eV), and C═O bonds (~288.3 eV). The decrease in the C−O and C═O peak intensity observed in the C 1s spectrum of rGO (Figure 1g) compared to that of the GO is consistent with GO reduction. Note that there are remaining C−O and C═O functional groups in the rGO-PAA after the reduction process, some of which are attributed to mechanical strength-enhancing cross-links between the GO and PAA.[33]

The XPS results are corroborated by X-ray diffraction (XRD; Figure S3) and Raman spectroscopy (Figure S4) analysis. Following GO-PAA reduction by HI vapor and thermal annealing, the characteristic (001) peak (2θ = 7.4°; d-spacing = 11.9 Å) of GO observed in the GO-PAA spectrum disappears, and the rGO-PAA XRD shows only a broad peak centered at around 2θ = 21° that matches closely to the spectrum of only PAA (Figure S3); this observation is consistent with the reduction of GO to rGO.[33] Furthermore, the Raman spectra of GO-PAA and rGO-PAA (Figure S4 and Table S1) are consistent with previous reports characterizing the reduction of GO to rGO, as evidenced by a decrease in the I_D/I_G ratio for rGO-PAA (I_D/I_G = 1.1) compared to GO-PAA

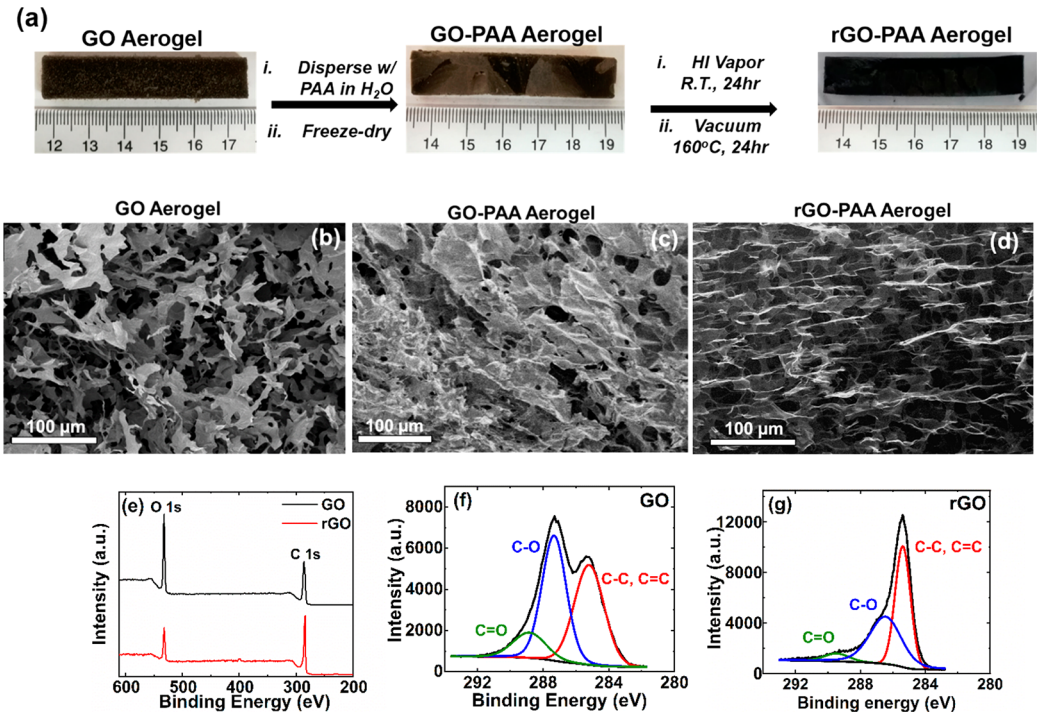

Figure 1. (a) Steps of forming the rGO-PAA aerogel from GO. Cross-sectional SEM images of the (b) GO aerogel, (c) GO-PAA aerogel before reduction and cross-linking, and (d) rGO-PAA aerogel following HI reduction and thermal cross-linking. (e) XPS survey spectra of GO (black trace) and rGO (red trace). (f) C 1s spectrum of GO and (g) C 1s spectrum of rGO.

DOI: 10.1021/acsaem.8b02007
ACS Appl. Energy Mater. 2019, 2, 905−912

(I_D/I_G = 1.4) that indicates a partial restoration of sp^2 hybridization in the carbon framework following reduction (i.e., reduction of oxygen-containing groups/sp^3-type carbon and less disorder in the rGO-PAA).[37,38]

The porosity and large pore-diameters provide for slurry-infiltration, i.e., circumvention of the lengthy steps of coprecipitation, hydrothermal, or chemical deposition that are commonly used in 3D electrode fabrication.[10] The rGO-PAA is infiltrated with a desired active-material loading by simply changing the slurry concentration, and its durability and elasticity provide for compression by calendaring (see stress–strain curves and digital images in Figures S5 and S6, respectively). To describe the LTO and NCM electrodes with various parameters, we have adopted the following nomenclature: the acronym for the active material (NCM or LTO) is followed by the supporting current collector (Al foil = "Al"; Cu foil = "Cu"; or rGO-PAA = "rGO") and finally the thickness of the electrode (μm). For example, LTO-rGO-31 refers to an electrode composed of LTO supported on rGO-PAA compressed to 31 μm. Or, NCM-Al-62 would refer to NCM supported on an Al foil current collector compressed to 62 μm electroactive-film thickness (electrode parameters displayed in Table 1a, b).

Figure 2 shows representative cross-sectional SEM images of LTO-rGO (Figure 2a and 2b) and NCM-rGO (Figure 2c and 2d) with an active-material loading of ~25–30 mg cm^{-2}. As displayed in Figure 2a and 2c, the uncompressed LTO-rGO (Figure 2a) and NCM-rGO (Figure 2c) composites show strong interaction between the active material and the rGO-PAA skeleton while still preserving the pore template for electrolyte transport. Following compression, the LTO-rGO-125 (Figure 2b) and NCM-rGO-130 (Figure 3d) show no observable cracks or defects while achieving overall electrode densities as high as 2–3 g cm^{-3}, approaching those used in practical applications with metal-foil electrodes (bare rGO-PAA parameters as a function of thickness in Table S2).[3−9] Cross-sectional SEM/EDX images (Figure S7–S10) confirm the effective distribution of LTO and NCM in both the low-loading (~3–4 mg cm^{-2}, 40 μm) and high-loading rGO-PAA electrodes (~25–30 mg cm^{-2}, 125–130 μm).

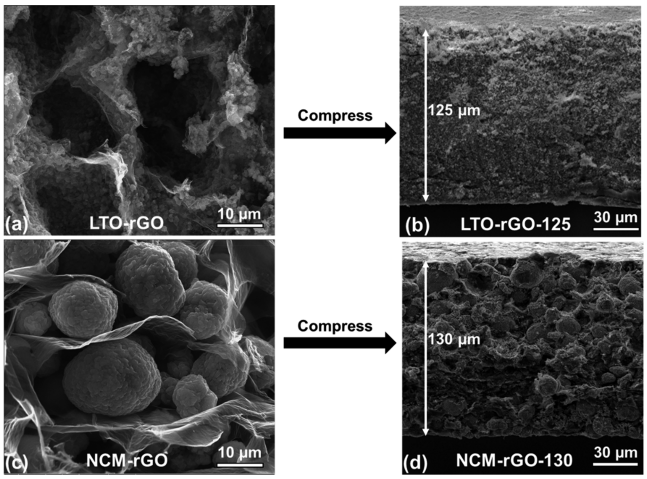

Figure 2. Cross-sectional SEM images of (a,b) LTO-rGO-125 and (c,d) NCM-rGO-130. (a) LTO-rGO-125 after loading rGO-PAA with LTO but before compression. (b) LTO-rGO-125 after compressing to ~125 μm. (c) NCM-rGO-130 after loading rGO-PAA with NCM but before compression. (d) NCM-rGO-130 after compressing to ~130 μm.

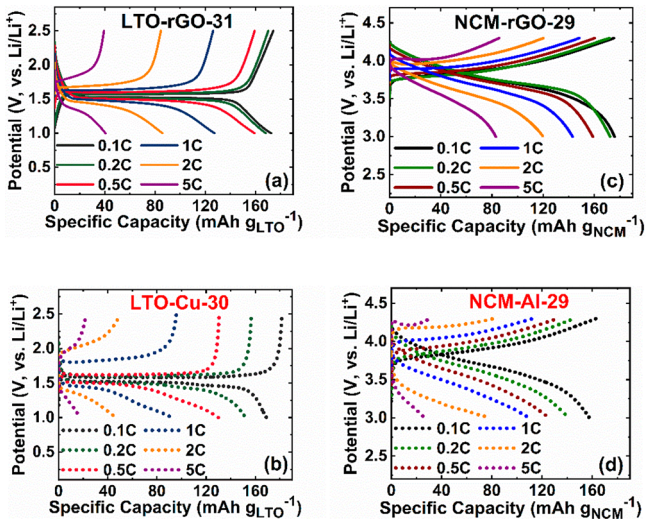

Figure 3. Charge–discharge profiles of (a) LTO-rGO-31, (b) LTO-Cu-30, (c) NCM-rGO-29, and (d) NCM-Al-29 as a function of C-rate.

The cyclic voltammogram (CV) of the rGO-PAA substrate alone (without the loading of active material) establishes its utility as a current collector through the 1.0–4.3 V (vs Li/Li^+) potential range, sufficient for either LTO or NCM electrodes (Figure S11a).

The charge–discharge profiles in Figure 3 illustrate that while all the thin electrodes perform similarly at 0.1C, the rGO-PAA electrodes are superior at 1 C. Comparatively, the LTO-rGO-31 electrode has a capacity retention of 75% of its original 0.1 C capacity (Figure 3a) versus only 54% for the LTO-Cu-30 electrode (Figure 3b). The capacity retention at 1 C of the NCM electrodes is 81% for NCM-rGO-29 (Figure 3c) and 69% for NCM-Al-29 (Figure 3d). Even at this low electroactive-material loading of ~3–4 mg cm^{-2}, the rGO-PAA provides an advantage over the analogous metal-foil electrodes.

Consideration of practical electrode capacities requires inclusion of the mass and volume of the film additives and current collectors (e.g., the capacity normalized to the total mass and volume of the electrode) used in electrode fabrication.[3−9] Desirably, switching from Al or Cu foil to the rGO-PAA current collector increases the weight fraction of active material in the electrode due to the dramatic reduction in current-collector weight (~6 mg cm^{-3} for rGO-PAA vs 2700 mg cm^{-3} for Al foil and 8940 mg cm^{-3} for Cu foil). The increase in active-material weight fraction is most significant at low active-material loadings (i.e., when the proportional weight of the current-collector is highest), with the LTO weight fraction increases from 23% in LTO-Cu-30 to 60% in LTO-rGO-31 and that of the NCM from 42% for NCM-Al-29 to 64% for NCM-rGO-29.

Figure 4 displays the electrode-specific capacities of the LTO and NCM electrodes at different loading/thickness (displayed in Table 1a and b). The charge–discharge profiles at 0.1 C for LTO (Figure 4a and b) and NCM (Figure 4d and e) show that on all current collectors the electrode-level capacity increases with the electroactive-material loading. The largest increase in electrode-level capacity is observed when transitioning from ~30 μm (3–4 mg cm^{-2}) to ~65 μm (12–13 mg cm^{-2}) for

DOI: 10.1021/acsaem.8b02007
ACS Appl. Energy Mater. 2019, 2, 905–912

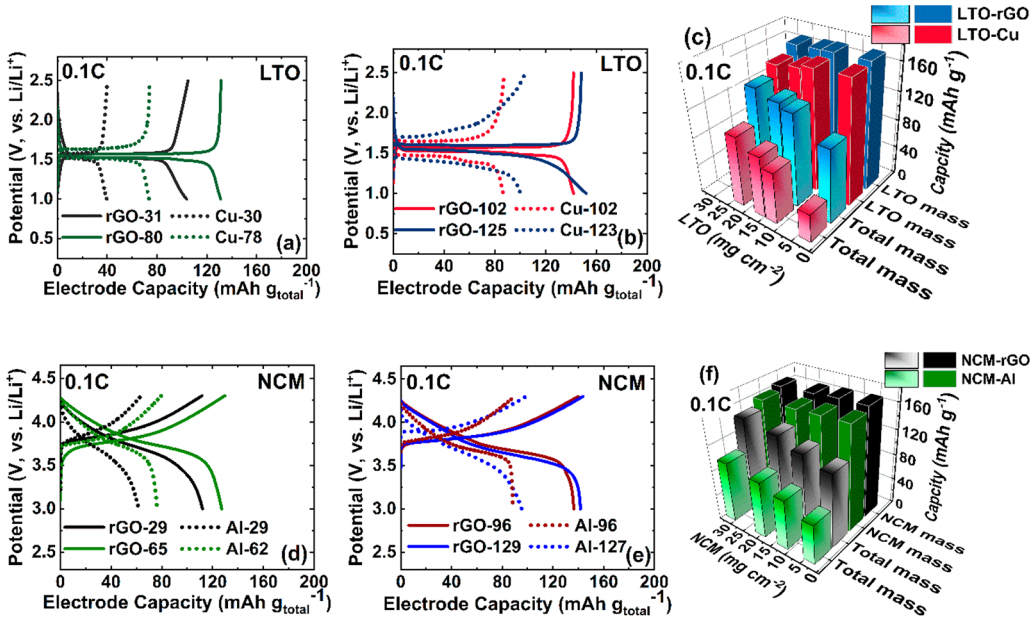

Figure 4. Charge−discharge profiles at 0.1 C for (a) LTO-rGO-31/80 vs LTO-Cu-30/78, (b) LTOrGO-102/125 vs LTO-Cu-102/123, (d) NCM-rGO-29/65 vs NCM-Al-29/62, and (e) NCM-rGO-96/129 vs NCM-Al-127. Capacity calculated from the total mass of the electrode including its electroactive material, binder, conductive additive, and current collector. (c) A comparison of the capacity normalized to the active-material mass (solid bars) and the total electrode mass (faded bars) at 0.1 C for LTO-rGO (blue)/LTO-Cu (red). (f) A comparison of the capacity normalized to the active-material mass (solid bars) and the total electrode mass (faded bars) at 0.1 C for NCM-rGO (black)/NCM-Al (green) as a function of active-material loading.

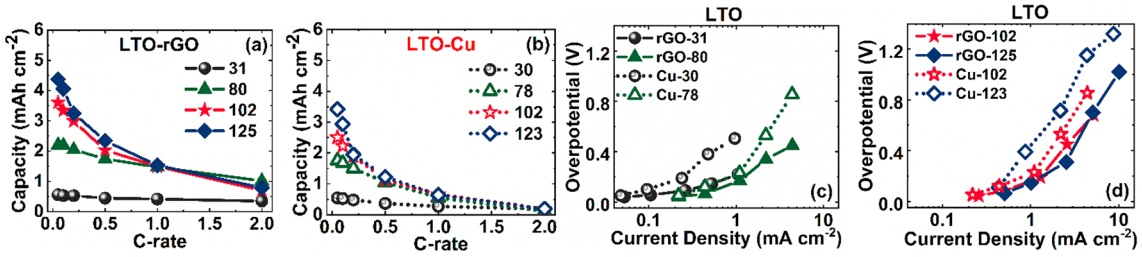

Figure 5. Areal rate capability of (a) LTO-rGO and (b) LTO-Cu as a function of LTO loading/thickness. Overpotential as a function of current density for (c) LTO-rGO-31/80 versus LTO-Cu-30/78 and (d) LTO-rGO-102/125 versus LTO-Cu-102/123.

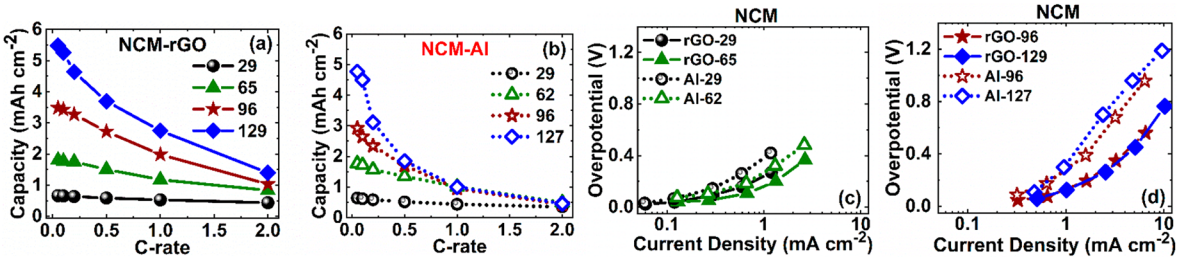

Figure 6. Areal rate capability of (a) NCM-rGO and (b) NCM-Al as a function of NCM loading/film thickness. Overpotential as a function of current density for (c) NCM-rGO-29/65 versus NCM-Al-29/62 and (d) NCM-rGO-96/129 versus NCM-Al-96/127.

NCM and ∼80 μm (12−13 mg cm^{-2}) for LTO because of the significant decrease in proportional current collector weight, which is consistent with previous reports investigating electrode loading/thickness effects.[3−7] The benefit of replacing the metal foils with rGO-PAA at the electrode level is evident when comparing the active-material capacity to the electrode-level capacity for LTO (Figure 4c) and NCM (Figure 4f). Although the capacity based on the active-material mass at 0.1 C is similar between analogous metal-foil and rGO-PAA electrodes, the large decrease in the current collector weight causes LTO-rGO-31 and NCM-rGO-29 to outperform even the thickest LTO-Cu-123 and NCM-Al-127 electrodes when the entire electrode weight is considered.

When the C-rate is increased such that Li^+ transport limitations adversely affect the reversible areal capacity, the advantage of the rGO-PAA becomes increasingly apparent for both LTO (Figure 5) and NCM (Figure 6). Albeit there is a decline in rate capability as the mass loading is increased regardless of the current collector used, employing a Cu foil current collector and increasing the thickness and mass loading

DOI: 10.1021/acsaem.8b02007
ACS Appl. Energy Mater. 2019, 2, 905−912

above 80 μm and 12 mg cm^{-2} for LTO-Cu is accompanied by a decrease in rate capability and at 0.5 C no additional capacity is gained by increasing the mass loading (curve overlap in Figure 5b). In contrast, using thicker electrodes of LTO on the rGO-PAA current collector show a relative capacity advantage even at 1 C (curve overlap in Figure 5a). More impressively, a thicker NCM-rGO electrode provides an increase in areal capacity at all C-rates tested (Figure 6a), while the areal capacity is diminished at 1 C in the thicker NCM-Al electrode (curve overlap in Figure 6b).

The improvement in rate capability facilitated by the rGO-PAA current collector can be understood by comparing the overpotential as a function current density (C-rate) for LTO (Figure 5c and 5d) and NCM (Figure 6c and 6d). For each set of comparable electrodes (i.e., similar mass loading and thickness) the rGO-PAA-supported electrodes show lower overpotentials at all current densities tested for both LTO (Figure 5c and 5d) and NCM (Figure 6c and 6d). In support of these results, cyclic voltammograms show smaller peak separations consistent with a smaller transport limitation (LTO, Figure S12 and Table S3; NCM, Figure S13 and Table S4) and the electrochemical impedance spectra (EIS) (LTO, Figure S14–S15 and Table S5; NCM, Figure S16–S17 and Table S6) show a lower charge-transfer resistance for the rGO-PAA electrodes versus the metal-foil electrodes. Plotting of the imaginary resistance versus the inverse square root of the angular frequency in the low-frequency region of the EIS spectra for the LTO (Figure S15) and NCM (Figure S17) shows, as expected, that the rGO-PAA increases the participating surface area 1.5-fold (eqs S1 and S2) for LTO-rGO and 1.7-fold for NCM-rGO compared to the participating surface areas of LTO-Cu and NCM-Al, respectively.

The high compressibility of the composite rGO-PAA electrodes also provides a volume advantage via the absence of the Al foil (16 μm thick) and Cu foil (11 μm thick), thereby enabling a ~25% increase in volumetric capacity at 0.1 C (Figure S18). At low power density, increasing the mass loading of LTO (Figure 7a and 7b) and of NCM (Figure 7c and 7d) results in volumetric energy densities as high as 625 Wh L^{-1} for LTO-rGO-125 (Figure 7b) and 1723 Wh L^{-1} for NCM-rGO-129 (Figure 7d). Notably, the thinner NCM-rGO-65 electrode approaches a volumetric energy density of 1200 Wh L^{-1} at low power density and retains ~800 Wh L^{-1} at a 1000 W L^{-1} volumetric power density (Figure 7c), comparing favorably with the results of Zheng et al.[7] who reported 1200 Wh L^{-1} at low power density for an NCM-Al electrode with a mass loading of 24.01 mg cm^{-2} and a thickness of 104 μm. The metrics obtained here indicate that the NCM-rGO-65 electrode provides for simultaneously avoiding transport and mechanical limitations that currently plague thick LIB electrodes.[3−9] Note that the volumetric energy densities discussed here are calculated from the volume of only the LTO and NCM electrodes and does not take into consideration the entire volume of the cell (e.g., Li-metal, separator, etc.).

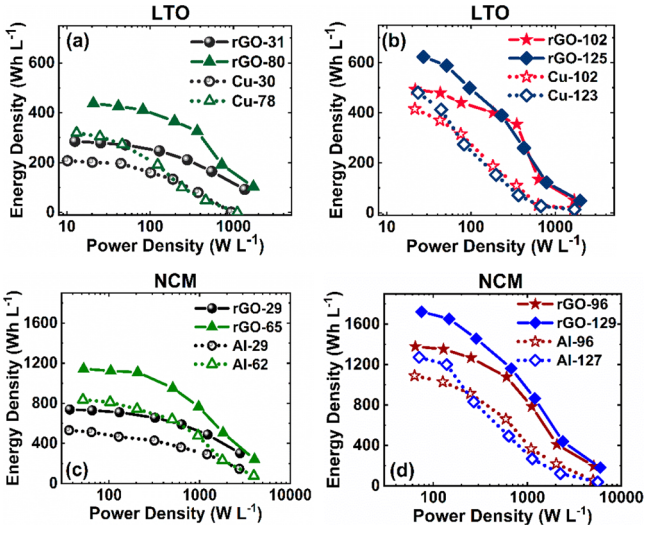

Figure 7. Ragone plots for LTO and NCM electrodes as a function of electrode thickness: (a) LTO-rGO-31/80 vs LTO-Cu-30/78, (b) LTO-rGO-102/125 vs LTO-Cu-102/123, (c) NCM-rGO-29/65 vs NCM-Al-29/62, and (d) NCM-rGO-96/129 vs NCM-rGO-96/127.

The electrochemical stability of the rGO-PAA was further evaluated by cycle stability tests at 0.5 C for 200 cycles (Figure 8). Comparison of the capacity retention of LTO-rGO

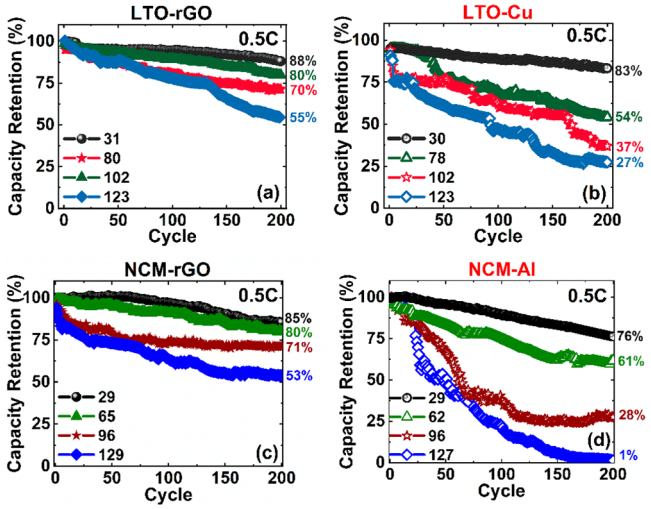

Figure 8. Cycling stability at 0.5 C for (a) LTO-rGO, (b) LTO-Cu, (c) NCM-rGO, and (d) NCM-Al.

electrodes (Figure 8a) with that of LTO-Cu electrodes (Figure 8b) shows improvements respectively by 5%, 26%, 33%, and 28% in order of increasing electrode thickness (Table 1a). The improvement for NCM is even more pronounced; at low thickness/loading, the NCM-rGO-29 electrode (Figure 8c) shows a 9% gain in capacity retention over the NCM-Al-29 electrode (Figure 8d) after 200 cycles, and the improvement increases to 19% for NCM-rGO-65, 43% for NCM-rGO-96, and 51% for NCM-rGO-129 compared to the NCM-Al counterparts. These results suggest that the rGO-PAA current collector is not prone to degradation during cycling and helps to mitigate the instability of the LTO and NCM at high loadings by providing an elastic and conductive skeleton to buffer volume change and improve electrical connection throughout the film during prolonged cycling.

4. CONCLUSIONS

Replacement of the conventional aluminum- and copper-foil current collectors of LIB electrodes by lightweight, porous, elastic, compressible, and free-standing rGO-PAA (rGO) aerogels obviates the dependency of film additives for electrode performance while simultaneously increasing (a) the optimal

DOI: 10.1021/acsaem.8b02007
ACS Appl. Energy Mater. 2019, 2, 905−912

thickness and mass loading of electroactive material per unit area, (b) both the volumetric and gravimetric energy density at low and intermediate power density, and (c) the capacity retention over prolonged cycling at a 0.5 C specific current.

The electrochemical performance of LTO-rGO and NCM-rGO electrodes with densities of 2−3 g cm^{-3} and thicknesses ranging from 30 to 130 μm (mass loading = 3−30 mg cm^{-2}) were compared with their copper and aluminum foil counterparts, LTO-Cu, and NCM-Al. Switching to the ∼6 mg cm^{-3} density rGO-PAA current collector from Al foil (2700 mg cm^{-3}) and Cu foil (8940 mg cm^{-3}) drastically reduced the proportional current collector weight and volume. Because of the reduced current collector volume, the volumetric energy density of cells made with lithium foil anodes reached 1723 Wh L^{-1} for NCM-rGO-130 and 625 Wh L^{-1} for LTO-rGO-125, and impressively, a thinner NCM-rGO electrode compressed to 65 μm (12−13 mg cm^{-2}) achieved ∼800 Wh L^{-1} at a specific volumetric power of 1000 W L^{-1}.

Overall, the rGO-PAA current collector provided for thinner electrodes without compromising the capacity. The reduced current collector weight enabled even the thinnest LTO-rGO and NCM-rGO (∼3−4 mg cm^{-2}) electrodes to outperform thickest LTO-Cu and NCM-Al electrodes (∼25−30 mg cm^{-2}) at the electrode level, and the conductive and elastic rGO-PAA improved the cycle stability of the LTO and NCM over 200 cycles at 0.5 C. Further optimization in the rGO-PAA system is required to understand the influence of electrode porosity on the rate capability and cycle stability of high tap density LIB electrodes, which is currently being investigated in our laboratories.

■ ASSOCIATED CONTENT

Supporting Information

The Supporting Information is available free of charge on the ACS Publications website at DOI: 10.1021/acsaem.8b02007.

Characterization of GO platelets (AFM), rGO-PAA aerogels (SEM), and composite LTO-rGO and NCM-rGO electrodes (SEM/EDX); density and areal mass measurements of bare rGO-PAA aerogels as a function of thickness; XRD patterns of PAA, GO-PAA, and rGO-PAA; Raman spectra of PAA, GO-PAA, and rGO-PAA; mechanical stress−strain measurements for rGO and rGO-PAA aerogels; digital images showing flexibility/foldability of rGO-PAA; cyclic voltammograms and electrochemical impedance spectroscopy analysis of bare rGO-PAA, LTO-rGO, LTO-Cu, NCM-rGO, and NCM-Al; volumetric charge−discharge curves for all electrodes at 0.1 C; thermogravimetric analysis (TGA) of GO-PAA and rGO-PAA; and SEM images of LTO and NCM particles used in this study (PDF)

■ AUTHOR INFORMATION

Corresponding Authors

*E-mail: mullins@che.utexas.edu.
*E-mail: cellison@umn.edu.

ORCID

Adam Heller: 0000-0003-0181-1246
Christopher J. Ellison: 0000-0002-0393-2941
C. Buddie Mullins: 0000-0003-1030-4801

Author Contributions

The manuscript was written through contributions of all authors. All authors have given approval to the final version of the manuscript.

Funding

The authors gratefully acknowledge the generous and continued support of the Welch Foundation through grants F-1131 (AH) and F-1436 (CBM), as well as the National Science Foundation via Grant CBET-1603491. The authors also thank Celgard for generously providing membrane separators. Parts of this work were carried out in the Characterization Facility at the University of Minnesota, which receives partial support from the National Science Foundation through the MRSEC program.

Notes

The authors declare no competing financial interest.

■ REFERENCES

(1) Goodenough, J. B.; Park, K.-S. S. The Li-Ion Rechargeable Battery: A Perspective. *J. Am. Chem. Soc.* **2013**, *135*, 1167−1176.
(2) Blomgren, G. E. The Development and Future of Lithium Ion Batteries. *J. Electrochem. Soc.* **2017**, *164*, A5019−A5025.
(3) Gallagher, K. G.; Trask, S. E.; Bauer, C.; Woehrle, T.; Lux, S. F.; Tschech, M.; Lamp, P.; Polzin, B. J.; Ha, S.; Long, B.; Wu, Q.; Lu, W.; Dees, D. W.; Jansen, A. N. Optimizing Areal Capacities through Understanding the Limitations of Lithium-Ion Electrodes. *J. Electrochem. Soc.* **2016**, *163*, A138−A149.
(4) Wood, D. L.; Li, J.; Daniel, C. Prospects for Reducing the Processing Cost of Lithium Ion Batteries. *J. Power Sources* **2015**, *275*, 234−242.
(5) Singh, M.; Kaiser, J.; Hahn, H. Thick Electrodes for High Energy Lithium Ion Batteries. *J. Electrochem. Soc.* **2015**, *162*, A1196−A1201.
(6) Du, Z.; Wood, D. L.; Daniel, C.; Kalnaus, S.; Li, J. Understanding Limiting Factors in Thick Electrode Performance as Applied to High Energy Density Li-Ion Batteries. *J. Appl. Electrochem.* **2017**, *47*, 405−415.
(7) Zheng, H.; Li, J.; Song, X.; Liu, G.; Battaglia, V. S. A Comprehensive Understanding of Electrode Thickness Effects on the Electrochemical Performances of Li-Ion Battery Cathodes. *Electrochim. Acta* **2012**, *71*, 258−265.
(8) Andre, D.; Kim, S.-J.; Lamp, P.; Lux, S. F.; Maglia, F.; Paschos, O.; Stiaszny, B. Future Generations of Cathode Materials: An Automotive Industry Perspective. *J. Mater. Chem. A* **2015**, *3*, 6709−6732.
(9) Choi, J. W.; Aurbach, D. Promise and Reality of Post-Lithium-Ion Batteries with High Energy Densities. *Nat. Rev. Mater.* **2016**, *1*, 16013.
(10) Cha, H.; Kim, J.; Lee, Y.; Cho, J.; Park, M. Issues and Challenges Facing Flexible Lithium-Ion Batteries for Practical Application. *Small* **2018**, *14*, 1702989−1703007.
(11) Nishide, H.; Oyaizu, K. Toward Flexible Batteries. *Science (Washington, DC, U. S.)* **2008**, *319*, 737−738.
(12) Li, L.; Wu, Z.; Yuan, S.; Zhang, X.-B. Advances and Challenges for Flexible Energy Storage and Conversion Devices and Systems. *Energy Environ. Sci.* **2014**, *7*, 2101−2122.
(13) Abe, H.; Kubota, M.; Nemoto, M.; Masuda, Y.; Tanaka, Y.; Munakata, H.; Kanamura, K. High-Capacity Thick Cathode with a Porous Aluminum Current Collector for Lithium Secondary Batteries. *J. Power Sources* **2016**, *334*, 78−85.
(14) Aguiló-Aguayo, N.; Espiñeira, P. P.; Manian, A. P.; Bechtold, T. Three-Dimensional Embroidered Current Collectors for Ultra-Thick Electrodes in Batteries. *RSC Adv.* **2016**, *6*, 69685−69690.
(15) Wang, J. S.; Liu, P.; Sherman, E.; Verbrugge, M.; Tataria, H. Formulation and Characterization of Ultra-Thick Electrodes for High Energy Lithium-Ion Batteries Employing Tailored Metal Foams. *J. Power Sources* **2011**, *196*, 8714−8718.

DOI: 10.1021/acsaem.8b02007
ACS Appl. Energy Mater. 2019, 2, 905−912

(16) Jiang, Y.; Jiang, L.; Wu, Z.; Yang, P.; Zhang, H.; Pan, Z.; Hu, L. In Situ Growth of $(NH_4)_2V_{10}O_{25}\cdot 8H_2O$ Urchin-like Hierarchical Arrays as Superior Electrodes for All-Solid-State Supercapacitors. *J. Mater. Chem. A* **2018**, *6*, 16308−16315.
(17) Li, H.; Ding, Y.; Ha, H.; Shi, Y.; Peng, L.; Zhang, X.; Ellison, C. J.; Yu, G. An All-Stretchable-Component Sodium-Ion Full Battery. *Adv. Mater.* **2017**, *29*, 1700898.
(18) Liu, W.; Chen, Z.; Zhou, G.; Sun, Y.; Lee, H. R.; Liu, C.; Yao, H.; Bao, Z.; Cui, Y. 3D Porous Sponge-Inspired Electrode for Stretchable Lithium-Ion Batteries. *Adv. Mater.* **2016**, *28*, 3578−3583.
(19) Xiao, H.; Pender, J. P.; Meece-Rayle, M. A.; De Souza, J. P.; Klavetter, K. C.; Ha, H.; Lin, J.; Heller, A.; Ellison, C. J.; Mullins, C. B. Reduced-Graphene Oxide/Poly(Acrylic Acid) Aerogels as a Three-Dimensional Replacement for Metal-Foil Current Collectors in Lithium-Ion Batteries. *ACS Appl. Mater. Interfaces* **2017**, *9*, 22641−22651.
(20) Park, Y.; Park, G.; Park, J.; Lee, J. Robust Free-Standing Electrodes for Flexible Lithium-Ion Batteries Prepared by a Conventional Electrode Fabrication Process. *Electrochim. Acta* **2017**, *247*, 371−380.
(21) Chen, Y.; Fu, K.; Zhu, S.; Luo, W.; Wang, Y.; Li, Y.; Hitz, E.; Yao, Y.; Dai, J.; Wan, J.; Danner, V. A.; Li, T.; Hu, L. Reduced Graphene Oxide Films with Ultrahigh Conductivity as Li-Ion Battery Current Collectors. *Nano Lett.* **2016**, *16*, 3616−3623.
(22) Sun, H.; Mei, L.; Liang, J.; Zhao, Z.; Lee, C.; Fei, H.; Ding, M.; Lau, J.; Li, M.; Wang, C.; Xu, X.; Hao, G.; Papandrea, B.; Shakir, I.; Dunn, B.; Huang, Y.; Duan, X. Three-Dimensional Holey-Graphene/Niobia Composite Architectures for Ultrahigh-Rate Energy Storage. *Science (Washington, DC, U. S.)* **2017**, *356*, 599−604.
(23) Zhou, Y.; Lee, Y.; Sun, H.; Wallas, J. M.; George, S. M.; Xie, M. Coating Solution for High-Voltage Cathode: AlF_3 Atomic Layer Deposition for Freestanding $LiCoO_2$ Electrodes with High Energy Density and Excellent Flexibility. *ACS Appl. Mater. Interfaces* **2017**, *9*, 9614−9619.
(24) Wang, Y.; He, Z.; Wang, Y.; Fan, C.; Liu, C.; Peng, Q.; Chen, J.; Feng, Z. Preparation and Characterization of Flexible Lithium Iron Phosphate/Graphene/Cellulose Electrode for Lithium Ion Batteries. *J. Colloid Interface Sci.* **2018**, *512*, 398−403.
(25) Lu, H.; Hagberg, J.; Lindbergh, G.; Cornell, A. $Li_4Ti_5O_{12}$ Flexible, Lightweight Electrodes Based on Cellulose Nanofibrils as Binder and Carbon Fibers as Current Collectors for Li-Ion Batteries. *Nano Energy* **2017**, *39*, 140−150.
(26) Hu, J. W.; Wu, Z. P.; Zhong, S. W.; Zhang, W. B.; Suresh, S.; Mehta, A.; Koratkar, N. Folding Insensitive, High Energy Density Lithium-Ion Battery Featuring Carbon Nanotube Current Collectors. *Carbon* **2015**, *87*, 292−298.
(27) Chen, C.; Zhang, Y.; Li, Y.; Kuang, Y.; Song, J.; Luo, W.; Wang, Y.; Yao, Y.; Pastel, G.; Xie, J.; Hu, L. Highly Conductive, Lightweight, Low-Tortuosity Carbon Frameworks as Ultrathick 3D Current Collectors. *Adv. Energy Mater.* **2017**, *7*, 1700595.
(28) Cao, S.; Feng, X.; Song, Y.; Liu, H.; Miao, M.; Fang, J.; Shi, L. In Situ Carbonized Cellulose-Based Hybrid Film as Flexible Paper Anode for Lithium-Ion Batteries. *ACS Appl. Mater. Interfaces* **2016**, *8*, 1073−1079.
(29) Hu, L.; La Mantia, F.; Wu, H.; Xie, X.; McDonough, J.; Pasta, M.; Cui, Y. Lithium-Ion Textile Batteries with Large Areal Mass Loading. *Adv. Energy Mater.* **2011**, *1*, 1012−1017.
(30) He, J.; Chen, Y.; Lv, W.; Wen, K.; Li, P.; Qi, F.; Wang, Z.; Zhang, W.; Li, Y.; Qin, W.; He, W. Highly-Flexible 3D Li2S/Graphene Cathode for High-Performance Lithium Sulfur Batteries. *J. Power Sources* **2016**, *327*, 474−480.
(31) Peng, H.-J.; Huang, J.-Q.; Zhang, Q. A Review of Flexible Lithium−sulfur and Analogous Alkali Metal−chalcogen Rechargeable Batteries. *Chem. Soc. Rev.* **2017**, *46*, 5237−5288.
(32) Jiang, Y.; Wu, Z.; Jiang, L.; Pan, Z.; Yang, P.; Tian, W.; Hu, L. Freestanding $CoSeO_3\cdot H_2O$ Nanoribbon/Carbon Nanotube Composite Paper for 2.4 V High-Voltage, Flexible, Solid-State Supercapacitors. *Nanoscale* **2018**, *10*, 12003−12010.
(33) Ha, H.; Shanmuganathan, K.; Ellison, C. J. Mechanically Stable Thermally Crosslinked Poly(Acrylic Acid)/Reduced Graphene Oxide Aerogels. *ACS Appl. Mater. Interfaces* **2015**, *7*, 6220−6229.
(34) Belharouak, I.; Sun, Y.-K.; Liu, J.; Amine, K. Li-$(Ni_{1/3}Co_{1/3}Mn_{1/3})O_2$ as a Suitable Cathode for High Power Applications. *J. Power Sources* **2003**, *123*, 247−252.
(35) Sun, Y.-K.; Chen, Z.; Noh, H.-J.; Lee, D.-J.; Jung, H.-G.; Ren, Y.; Wang, S.; Yoon, C. S.; Myung, S.-T.; Amine, K. Nanostructured High-Energy Cathode Materials for Advanced Lithium Batteries. *Nat. Mater.* **2012**, *11*, 942−947.
(36) Yuan, T.; Tan, Z.; Ma, C.; Yang, J.; Ma, Z. F.; Zheng, S. Challenges of Spinel $Li_4Ti_5O_{12}$ for Lithium-Ion Battery Industrial Applications. *Adv. Energy Mater.* **2017**, *7*, 1601625−1601650.
(37) Kaniyoor, A.; Ramaprabhu, S. A Raman Spectroscopic Investigation of Graphite Oxide Derived Graphene A Raman Spectroscopic Investigation of Graphite Oxide Derived Graphene. *AIP Adv.* **2012**, *2*, 032183−032197.
(38) Hong, J. Y.; Bak, B. M.; Wie, J. J.; Kong, J.; Park, H. S. Reversibly Compressible, Highly Elastic, and Durable Graphene Aerogels for Energy Storage Devices under Limiting Conditions. *Adv. Funct. Mater.* **2015**, *25*, 1053−1062.

DOI: 10.1021/acsaem.8b02007
ACS Appl. Energy Mater. 2019, 2, 905−912